A NEW METHOD OF DYNAMIC AND STATIC STALL DETECTION USING INFRARED THERMOGRAPHY

A.D. Gardner*, C. C. Wolf†, M. Raffel‡

ABSTRACT

A new method of detecting flow separation for static and pitching airfoils is described, with application to the generation of stall maps for helicopter rotors. An airfoil is heated using a lamp and a high-speed infrared camera monitors the surface temperature. Subtracting consecutive images and performing a spatial standard deviation over a region of interest yields a single σDIT value which is used to detect boundary layer separation on the airfoil. The data can be analysed to identify attached flow (low values of σDIT) and separated flow (high values of σDIT). Although appropriate filtering can significantly improve the signal to noise ratio, the method is robust regarding the exact method of analysis and the unfiltered data is sufficiently clear to be analysed without additional processing. For the test airfoil used, stall was measured up to a pitching frequency of 5 Hz, and signal to noise ratios indicate that it should be possible to measure stall for a pitching frequency of 20 Hz for a carbon-fibre surface with the thermal properties used.

1 Introduction

Due to the nature of the problem, all helicopter main rotors in forward flight have areas of separated flow. For high-speed forward flight or highly loaded maneuvering flight the area of separated flow expands and the large dynamic loads associated with the stalled areas of the blade require a limitation of the flight envelope.

The investigation of helicopter blade stall involves the production of "stall maps" where the areas on the rotor disc which are stalled are geometrically described. These are currently most commonly produced by the investigation of pressure sensor data from sensors integrated into the rotor blades [3], but early investigations used rotating camera observations of tufts attached to an uninstrumented blade to produce the same result [9]. The technical complexity of instrumenting rotor blades has lead to the development of other methods of detecting stall for a wind tunnel test of a rotor, including using Particle Image Velocimetry (PIV) [10] and Pressure Sensitive Paint (PSP) [6]. PIV provides flow field data definitively proving stall for a single radial and azimuthal position, but without needing any treatment of the rotor blade. PSP provides pressure data on the surface of the rotor which can be correlated to stall, and requires painting the rotor blade, but can be performed after manufacture for any instrumented or uninstrumented blade.

Infrared cameras have long been used for flow analysis, with the observations of Thomann and Frisk [20] in 1967 being the first published experiments. For a long time the only applications were in hypersonic research due to the low sensitivity of the cameras available [8]. The first subsonic investigations by [2] used a measurement of the recovery temperature in transonic flow to measure boundary layer transition. The work of Quast [11] extended the application range by using a heated wall to measure heat transfer rather than recovery temperature, thus significantly increasing the signal available for measurement. Quast measured boundary layer transition and the laminar separation bubble at the boundary between laminar and turbulent boundary layer flow. Thin resistive heating films have since been used by a large number of groups including de Luca et al [5]. They showed that when the flow is separated over a laminar separation bubble on a Göttingen 797 airfoil that the convective cooling is significantly reduced and a warm area of separated flow can be detected and using an infrared camera. Astarita and Cardone [1] used the heated thin-foil method to investigate flow in a 108° sharp turn of a channel showing flow separation. An overview of some recent experiments separation and transition detection using these methods is given by Carlomagno and Cardone [4]. With the advent of high-speed infrared cameras, they have been used for the detection of boundary layer transition in the rotating system where that would not previously have been possible due to the camera framing time, including on a helicopter hovering in ground effect [17].

This paper will detail a new optical method for detecting flow separation on an airfoil, with the potential for gener-

*Corresponding Author. German Aerospace Center (DLR), Institute of Aerodynamics and Flow Technology, Bunsenstrasse 10, 37073 Göttingen, Germany. *tony.gardner@dlr.de*

†DLR-Institute of Aerodynamics and Flow Technology

‡DLR-Institute of Aerodynamics and Flow Technology

This paper was presented at the 42nd European Rotorcraft Forum, September 6-8, 2016, Lille, France

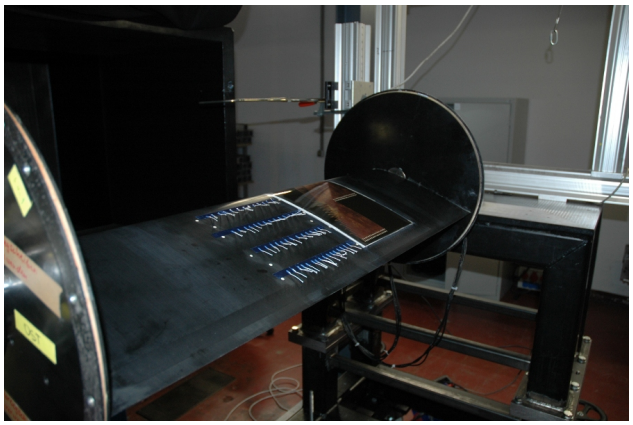

Figure 1: DSA-9A airfoil installed in the 1MG open test section. Flow is from left to right. Pictured are hot-films on the airfoil surface and tufts for flow visualisation

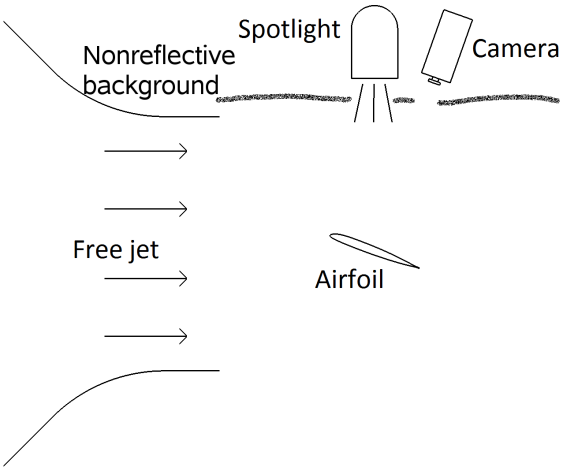

Figure 2: Sketch of the experimental arrangement.

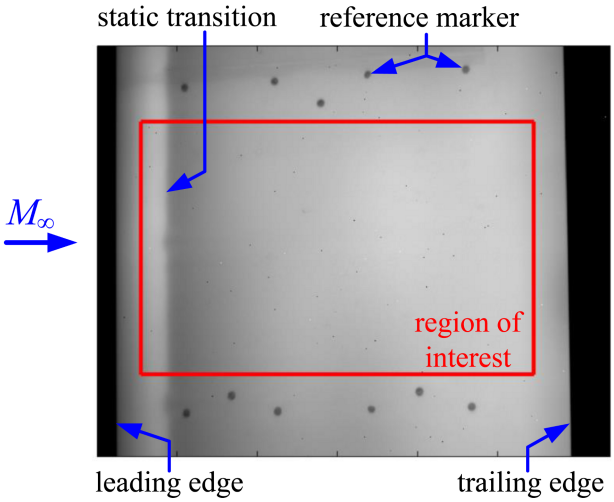

Figure 3: Example static image showing the sampling area on the airfoil

ating stall maps of highly loaded rotors without the technical complexity and costs of installing pressure sensors in the rotor blades. An example of the usage on a rotor can be fount in [13]. The method is based on image acquisition using the DIT method of Raffel et al. [12] and the ensemble-averaging flow analysis of Gardner and Richter [7]. The accuracy of the boundary layer transition position detected using DIT has been verified using a comparison to hot-film transition data and pressure-signal analysis [15]. Previous authors (with the exception of Raffel et al.) have concentrated on time-averaged (or static) flows and have analysed the temperature (or infrared image intensity) directly. Analysing differences between consecutive infrared images using Differential Infrared Thermography (DIT) was applied by Raffel et al. [12] to find dynamically varying transition positions in the rotating or nonrotating frames with infrared cameras. Raffel et al. also used the innovative technique of using spotlights to heat the surface without needing to apply a resistive heating film.

If nominally identical (or very similar) flow conditions are averaged, then the standard deviation (the differences between these flow conditions) is dominated by the effects of turbulent processes. Gardner and Richter [7] have shown that this can be used to identify the position of boundary layer transition on an airfoil using pressure sensor data. Further, the pressure sensor data of Gardner and Richter showed a much larger peak in standard deviation associated with flow separation. This peak can be used to identify areas of flow separation for either a statically inclined airfoil or a dynamically pitching airfoil.

2 Experiment and description of method

The same DSA-9A airfoil as investigated by Richter et al. [15] in the TWG transonic wind tunnel was installed in the 1MG wind tunnel, a low speed, open test section wind tunnel with flow of 50 m/s, see Fig. 1. The airfoil was instrumented with a single set of 50 Kulite pressure transducers installed in a single cut under the surface of the airfoil centerline. Hot-film sensors were mounted along a second cut, but were not used for the current experiment. The tufts in Fig. 1 were used for a quick identify points of interest, but not used during the main experiment and the airfoil used the end-plates shown, to improve the two-dimensionality of the flow. The airfoil is pitched sinusoidally at α=19$\pm$8° at f=2.5 Hz and the pressure data was sampled at 8000 samples per pitching period for 100 periods. The pressure data is phase-averaged over all periods and the mean and standard deviation in C_P (σC_P) is found for each phase angle.

The set-up for DIT is shown in Fig. 2. The airfoil in the center of the wind tunnel free-jet (static temperature 26°C) is heated by a 2 kW lamp from above the airfoil, which was adjusted to have a uniform heating of the area under observation. Under constant flow the surface temperature was measured to be 37±2°C using a handheld infrared thermometer. A high speed infrared (HSIR) camera (FLIR SC7750-L) was installed above the airfoil and observed the central part of the airfoil upper side. The HSIR camera had a spectral range of 8.0-9.4 μm detected by a Cadmium-Mercury-Telluride FPA detector with a resolution of 640x512 px. A 50 mm focal length lens with an aperture 2.0 was used. The data acquisition used an integration time of 200 μs, with an acquisition rate of f = 107 Hz. The camera was calibrated with a two-point calibration of the individual pixel sensitivity using a cold and hot hollow spherical half-shell held in front of the lens before each set of measurements. The DIT method evaluates intensity differences in the thermal images, and thus the conversion of intensity levels to temperature levels was not undertaken.

The surface properties of the airfoil have a significant effect on the infrared signal measured, as recently explored by Simon et al. [19]. The airfoil surface was made of carbon-fibre reinforced plastic with a black colour, with an estimated emissivity of E=0.95 [15]. An external layer of unreinforced resin was painted into the mould during manufacture, and this layer was polished after the airfoil was removed from the mould. The airfoil is made of two 3mm shells (top and bottom) constructed using the L285/H287 system of the firm Hexion, and the fiber volume is 45%. We do not have exact values for the thermal properties of the surface, but estimate the thermal conductivity through the shell as k_v=0.5 W/m/K and along the shell as k_h=7 W/m/K, density ρ=1180 kg/m^3 and specific heat capacity Cp=2300 J/kg/K. Thus the surface is relatively thermally nonconductive in the vertical direction. An important part of the setup is the reduction of reflections, since small reflections have a large effect in the difference images. The reflections were reduced by observing the airfoil without flow and adjusting a black cloth (noted in Fig. 2) so that reflections were not seen.

Figure 3 shows a sample individual infrared image taken for flow at a static angle of attack. The flow in this image is from left to right, and the airfoil leading and trailing edges are visible. Boundary layer transition is visible as a light/dark boundary in the image as the surface heat flux changes over the transition region, and dark marker dots (conductive silver paint which was polished smooth) are also visible. At the top of the image the edge of the hot-film foil (not used) is visible and the pressure taps are in a single cut between the two rows of markers with the Kulite XQ093 sensors installed underneath the surface. The pressure sensors do not affect the flow, except perhaps in the slight wiggle in the transition position halfway between the dots. To perform the analysis of the separated flow on a pitching airfoil 6000 infrared images were taken at 107 Hz, which amounts to data for 140 pitching cycles over 56 seconds of measurement time. The images were sorted into position along the cycle of the periodic movement, forming 300 bins in t/T. The data in each bin was then sorted in ascending time, so that the images nearest to each other were nearest in time and any effect of a temperature gradient over the measurement time would be reduced. Pairs of consecutive images were subtracted from each other to form n-1 DIT images in each bin of n IR images. Due to the relatively low frame rate of the camera compared to the pitching rate, pairs of "consecutive" images in the sorted data always came from different pitching cycles of the airfoil, thus the changes in the difference images indicate a shift from attached flow which is similar between different pitching cycles to separated flow which differs between pitching cycles.

An analysis window ("region of interest" in Fig. 3) was selected to avoid the edge effects of the airfoil and the reference markers. For the images in this paper, no mapping to compensate for the pitching motion was undertaken, since the maximum marker movement between α_{max} and α_{min} was 13 pixels, meaning that in each bin the maximum movement was less than 0.1 pixels. It was thus not felt that a mapping would improve the images. Experimentally it was shown that even when the number of bins was reduced to 75 that the signal-to-noise ratio did not increase, so it appears that the technique is not very sensitive to an exact mapping. Since no mapping was used, the dead/outlier pixels seen in Fig. 3 were also not compensated, but summed to zero during the differencing of two images for the DIT. The DIT images were then smoothed using a 3x3 pixel running average, which reduced the effect of pixel noise. For each DIT image the spatial standard deviation was calculated over the analysis window, with the signal from each pixel contributing equally to the standard deviation. This yields a single σDIT value for each DIT image, which is related to the non-uniformity of the flow's thermal footprint. For each bin the average spatial standard deviation was calculated, representing the combined information of 20 HSIR images in the case of dynamic pitching motions.

Variations on the evaluation method for the new images were tested and also found to work, as detailed later, but a reliable method for evaluating the images was:

1. Sort raw infrared images first by phase, then divide into bins and sort each bin in time.
2. Subtract consecutive images to form DIT images
3. Smooth DIT images
4. Define a spatial window
5. Compute the spatial standard deviation over the window
6. Average the standard deviation over each bin

For the static flow the number of bins is one, and a single standard deviation was acquired by averaging all 6000 IR images.

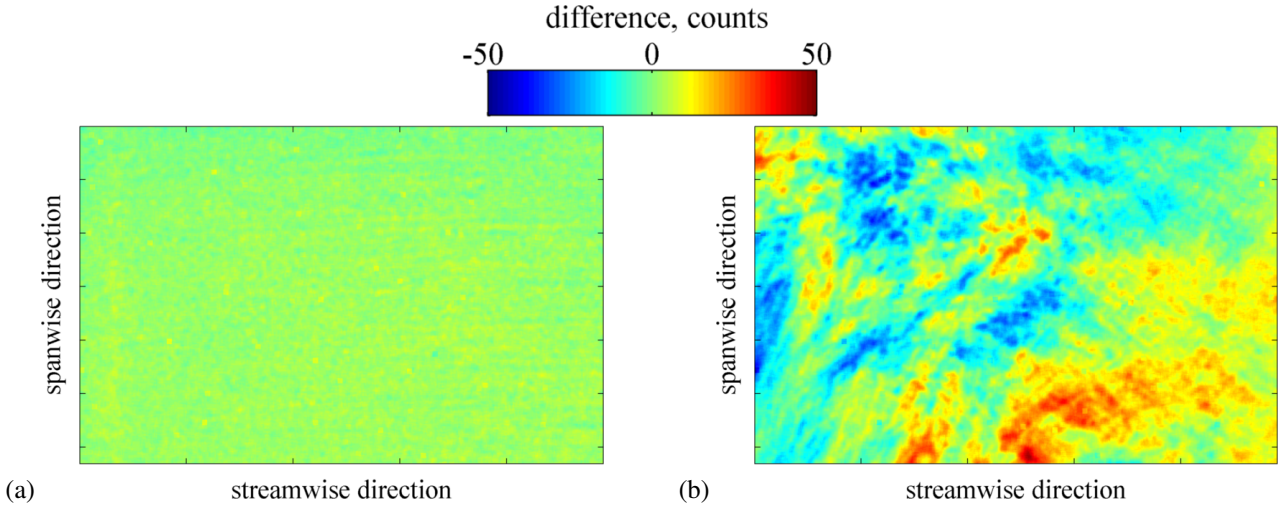

Figure 4: Example images using the standard deviation of the DIT images (a) Static, α=10° (b) Static, α=28°.

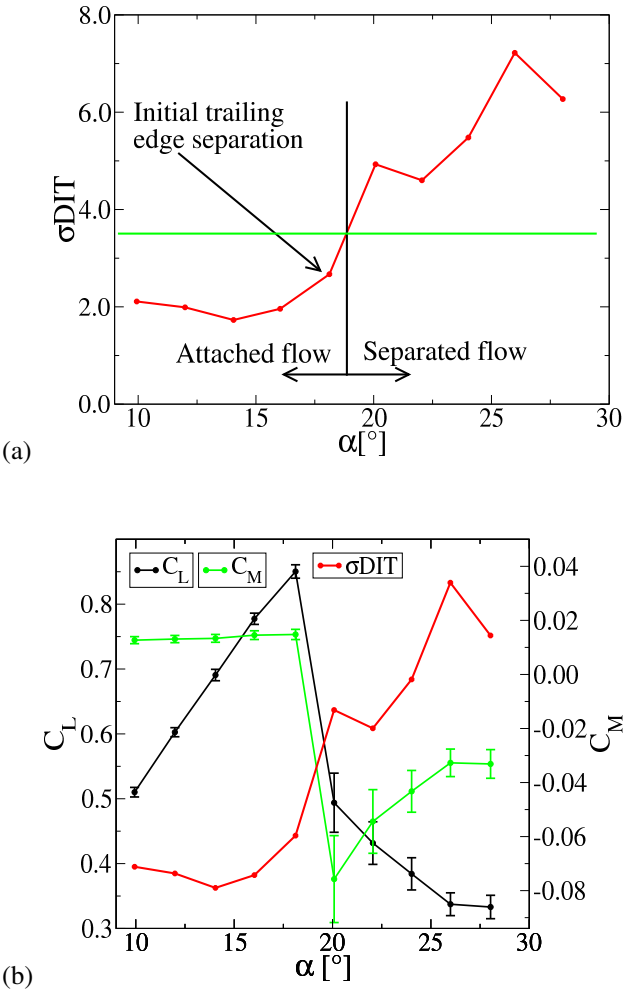

Figure 5: (a) Variation of the standard deviation of the difference signal with phase for a static point. (b) Comparison of σDIT data with C_L and C_M polars.

3 Static flow separation

For a statically inclined airfoil with flow at v=50 m/s, example DIT images are shown in Fig. 4. For the attached flow the DIT images show almost zero signal, indicating that the flow is quite uniform and unchanging, and that the differencing correctly compensates for unevenness in the individual images due to inhomogeneous structure, lighting, surface heating or emissivity. The residual signal is the image-to-image change in signal due to the airfoil vibration, changes in the wind tunnel flow, changes in temperature and lighting and sensor noise. In the DIT image for a statically inclined airfoil with separated flow the difference between attached and separated flow is readily visible to the naked eye, since the 3D structures in the separated flow correlate poorly between consecutive images.

If the σDIT values are plotted for a static polar, as seen in Fig. 5a, then a rise in σDIT is seen with the start of flow separation. The incipient start of trailing edge separation is seen as a small rise in σDIT from around 2 for attached flow, and when σDIT is greater than around 4 then the flow is separated. The exact value of σDIT depends on the image quality, bin size and filtering used, and thus it is the rise from a constant value of σDIT during attached flow rather than the absolute value of σDIT which indicates flow separation. The comparison with the integrated pressure data for C_L and C_M shows that the initial rise in σDIT is due to the start of a trailing edge separation (seen in the change in gradient of C_L), and that the abrupt rise in σDIT is due to flow separation. Flow separation in the static case can also be easily shown using other methods, and thus it is the dynamic pitching case which will be investigated in more detail.

4 Detection of dynamic stall

For the dynamically pitching airfoil at v=50 m/s, and α=19±8° at f=2.5 Hz, a dynamic stall condition is produced with generation of a leading edge dynamic stall vortex. The analysis of σDIT results in Fig. 6(a), showing a region with low σDIT associated with attached flow and a region of high σDIT associated with separated flow. As a comparison, the σC_P signal from a pressure sensor at x/c=0.10 on the suction side of the airfoil is included. In the σC_P signal, the passage of boundary layer transition over the sensor can be seen at t/T=0.092 (upstroke) and t/T=0.912 (downstroke), and it can be seen that the large signal in σC_P due to flow separation is comparable both in time and shape to the σDIT signal. The gradients in σC_P at the start and end of stall are higher than seen in σDIT, and as will be seen later, this is an effect of the large spatial area used for the σDIT signal. The fully separated flow shows a slightly increased level in σC_P compared to the attached flow. It is this effect which will be used in the DIT images to detect separated flow. The phase-averaged lift and pitching moments integrated from the pressure transducers (discretisation error $\ll$1%) are shown in Fig. 6(b) showing a sudden stall and the generation of a large negative pitching moment peak.

Points from the pressure sensors could be used to identify particular points on the σDIT graph. For attached flow, σDIT is low, and for separated flow σDIT is high, with a cutoff between the two states around σDIT=5, much higher than for the static case. From the analysis of the lift, pitching moment and pressure distributions, the following points could be clearly identified, as marked in Fig. 6:

1. Start of moment stall visible in C_M
2. Start of the trailing edge separation visible in the pressure distribution
3. Start of dynamic stall visible in the pressure distribution.
4. $C_{L_{max}}$
5. Dynamic stall vortex generated, starts to move downstream
6. $C_{M_{min}}$
7. Dynamic stall vortex over the airfoil trailing edge
8. $C_{L_{min}}$
9. Start of flow reattachment visible in the pressure distribution
10. Flow reattachment complete visible in the pressure distribution

The points 2,3,5,7,9 and 10 are extracted from the pressure distributions shown in Fig. 7, and the points 1,4,6,7 and 8 are from the integral forces in Fig. 6(b). The positions of the dynamic stall vortex are not always obvious from the individual points in Fig. 7 (see point 7 especially), but an analysis of the motion of the wave associated with the dynamic stall vortex allows its position to be clearly determined. The rising flank of the σDIT signal encompasses the whole dynamic stall process with the generation and

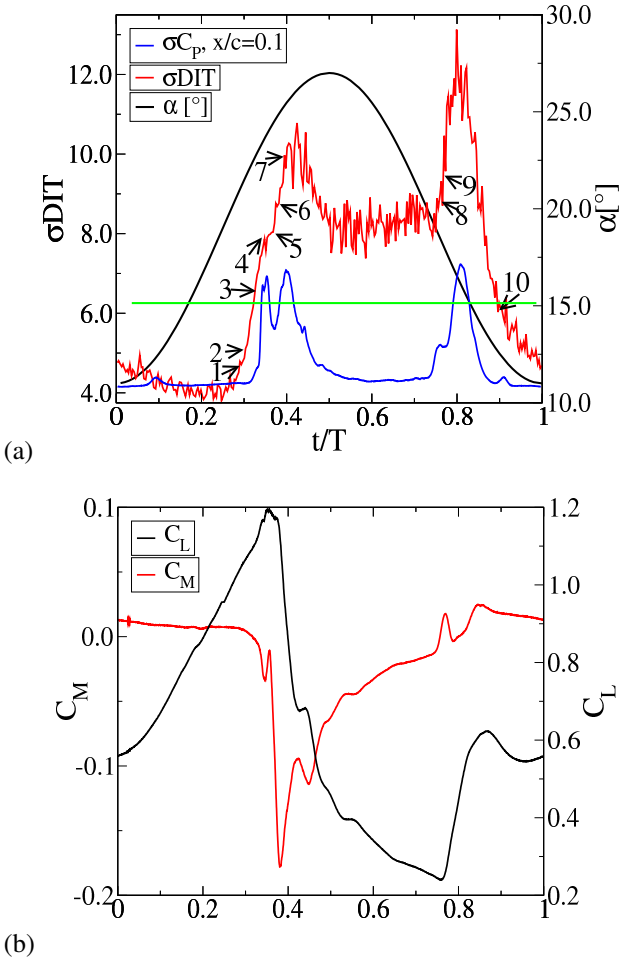

Figure 6: Variation of signal with phase for a dynamic point (a) the standard deviation of the DIT images, averaged over the large window with 3x3 spatial smoothing using 300 bins over a cycle (b) Phase-averaged lift and pitching moment integrated from the pressure sensors.

convection of the dynamic stall vortex from the airfoil The plateau in the middle of the peak is the region of fully separated flow, analogous to separated flow for a static airfoil. The flow reattachment starts at the rising flank of the second peak and continues until σDIT has dropped to the low level associated with attached flow.

A contrast to the analysis using the DIT can be found by investigating the mean value of the original images over the region of interest in Fig. 3. For the static test case, the temperature of the airfoil would be higher with separated flow as noted by many authors [8, 4]. For the dynamically pitching airfoil the temperature does not reach a steady state, but the temperature increases when the flow is separated due to the reduced cooling from the airflow, see the mean temperature over the region of interest shown in Fig. 8. It can be seen that as soon as the flow stalls (t/T=0.35), that the mean temperature has a positive gradient. At the point of reattachment (t/T=0.8), the cooling due to the flow is reasserted and the surface cools until it reaches equilibrium

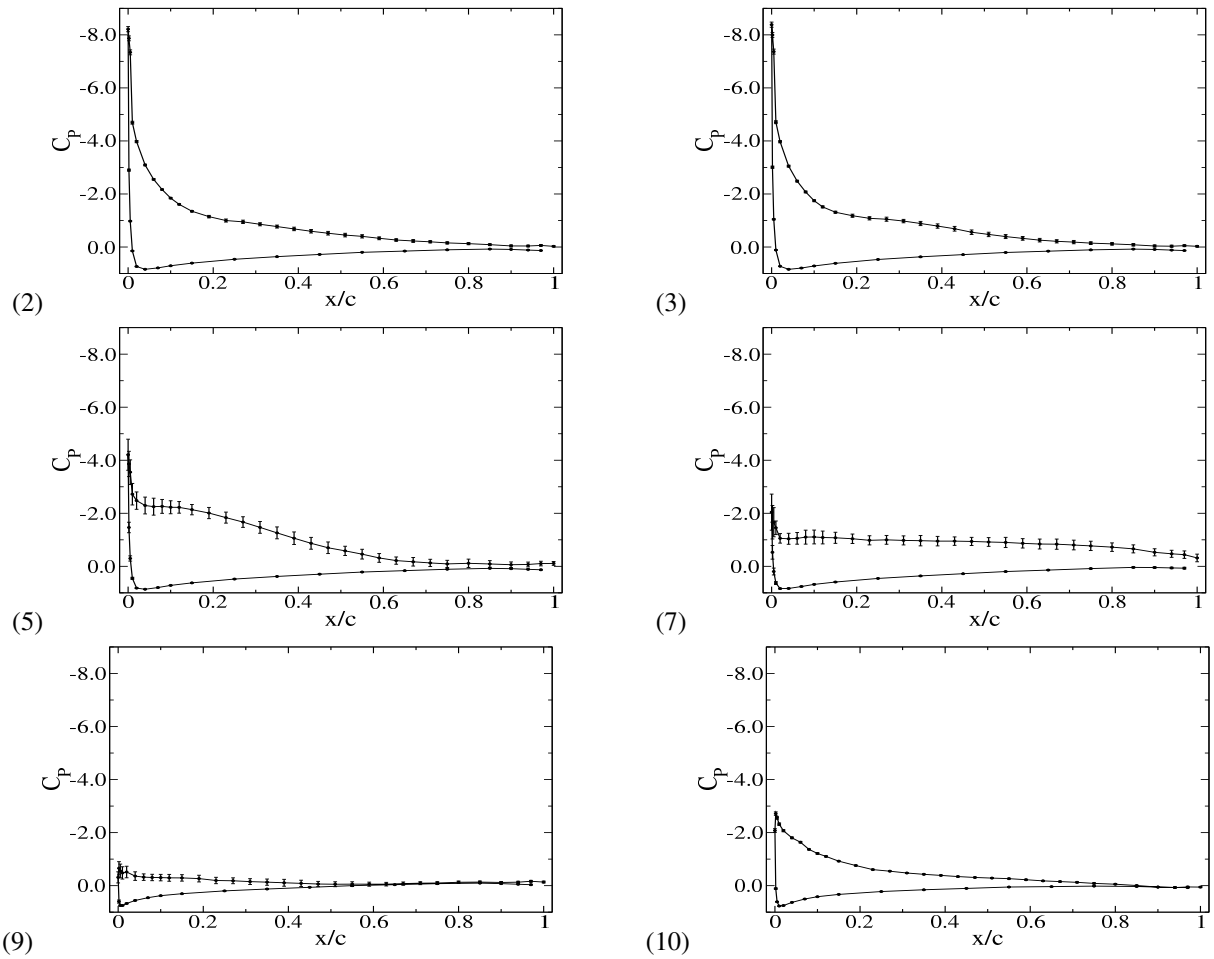

Figure 7: Phase-averaged pressure distributions with standard deviations corresponding to the points in Fig. 6

at t/T=0.1, whereafter the surface has a constant temperature until t/T=0.3. At his point a higher heat transfer than in the attached flow is present, causing the surface temperature to reduce. This higher heat transfer is associated with the region of dynamic stall, as seen by the falling flank of C_M in Fig. 6b and the rising flank of σDIT in Fig. 6a, and is related to the expansion of the trailing edge stall upstream, but the exact mechanism is not known at this time. Thus the analysis of stall in the dynamic system is also possible using the mean temperature, but since different parts of the stall process result in either a higher or lower cooling of the surface than the attached flow, neither a peak analysis nor a gradient analysis would allow a good determination of the times of separation. For this reason the analysis of σDIT is preferred as being simpler. As will be shown in the next section, the analysis of σDIT is also a robust and practical technique which is relatively insensitive to the exact algorithm used for the analysis.

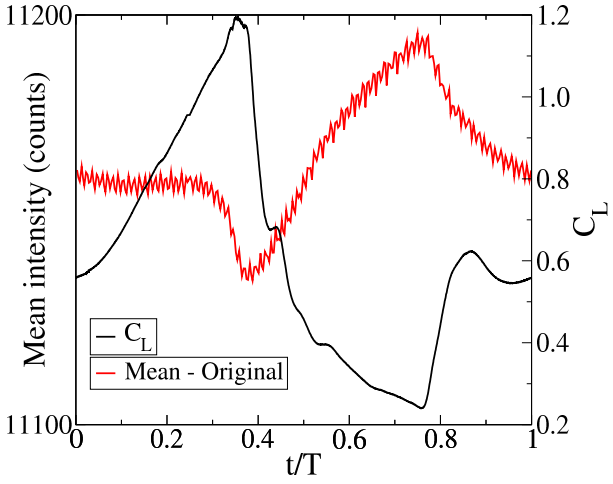

Figure 8: Variation of the mean over the original infrared images, averaged over the large window with 3x3 spatial smoothing using 300 bins over a cycle.

5 Sensitivity analysis

The algorithms used to produce the σDIT values are investigated in this section to show the sensitivity of the process to changes in the analysis method. The smoothing, sorting and binning, and temperature differences can all be analysed for their optimal settings. Additionally, the effect of pitching frequency is shown to be uncritical.

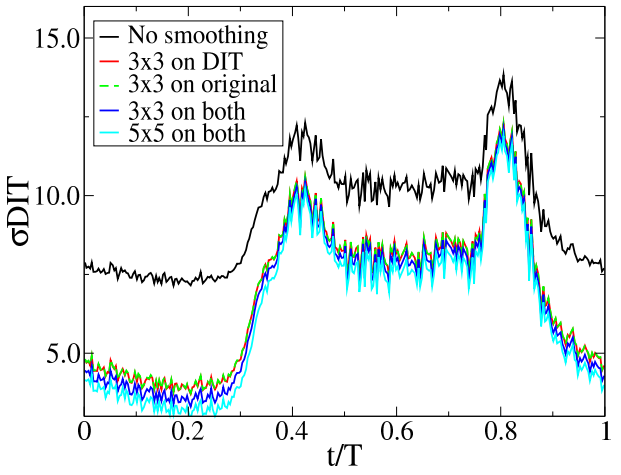

Figure 9: Comparison of σDIT for different spatial smoothing schemes using 300 bins over a cycle.

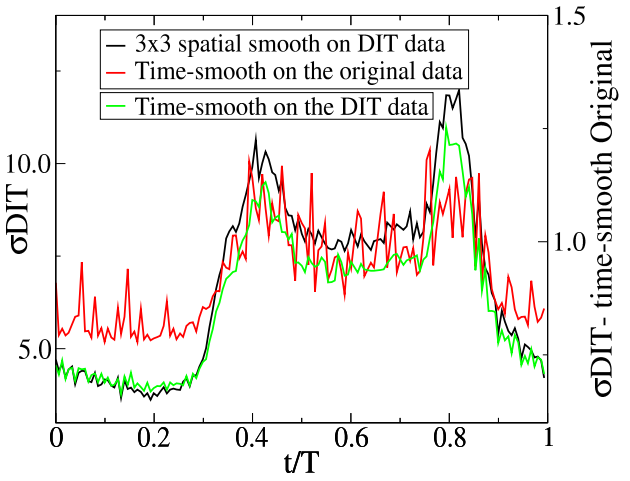

Figure 10: Comparison of σDIT for time-based and 3x3 spatial smoothing using 300 bins over a cycle.

Smoothing is used to improve the signal to noise ratio of the σDIT result. The effect of camera pixel noise can be reduced by either a spatial or a time smoothing, and a spatial filtering to remove small-scale structures and prefer large-scale structures selects more strongly for the difference between attached and separated flow. Figure 9 shows the use of spatial smoothing to improve the signal to noise ratio by averaging all of the original data in an NxN square onto the pixel in the middle of the square for the smoothed data. Without smoothing the black line has a signal to noise ratio of SN=1.8, if we divide the highest peak by the deepest trough after a 10-point moving average. Using the same method on the 3x3 pixel smoothing it can be seen that the signal to noise ratio increases to SN=3.0, regardless of whether the smoothing is performed on the original images or on the DIT data. Smoothing on both data sets improves the signal to noise ratio only marginally to SN=3.3. Using a larger 5x5 window improves the signal to noise ratio again to SN=3.6, but it can be seen that the main improvement was already in the original 3x3 smoothing. Thus for the investigations of other effects the 3x3 smoothing on the DIT data will be used to provide a constant reference point.

A second option for the smoothing is to smooth over time, where the results for a single pixel are smoothed using a moving average in time with a width of ±5 time steps. The results of this smoothing are seen in Fig. 10. If the smoothing is performed on the original data it is ineffective in improving the signal to noise ratio and greatly reduces the absolute value of σDIT, since the differences between consecutive images are reduced and the DIT is rendered ineffective. The result also suffers from quantization effects, since the differences between the two images are often less than one intensity count. If the time smoothing is performed after the image differencing is performed, a similar result to that for the 3x3 spatial smoothing is achieved with a signal to noise ratio of SN=2.7 produced. This indicates that the primary effect of the 3x3 spatial smoothing is

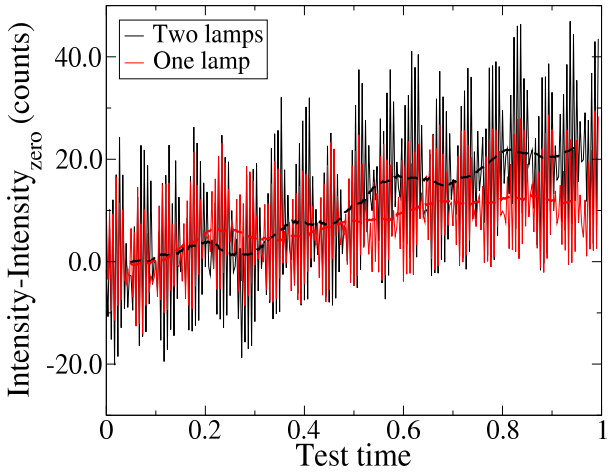

Figure 11: Temperature rise as IR camera intensity counts over the test time for two different heating cases. Thick lines are running averages.

a reduction of the pixel noise from the camera rather than a spatial filtering.

The investigations above were performed with 300 bins of images per cycle, sorted with a phase/time sort. This means that the data is first sorted by phase, and then the phase space divided into N bins. Each bin is then sorted in time. The hope was that the slow change in surface temperature over time would be best compensated by this method. Figure 11 shows the increase in temperature over time in infrared intensity counts for the single lamp used for the majority of tests. In this case an intensity increase of 12 counts over the test time of 56 seconds was seen. As seen in Fig. 8, the absolute intensity is around 11000 counts, so this represents a change of around 0.1%. As an alternative, A second lamp was additionally used to heat the airfoil and this resulted in an increase in temperature of 21 intensity counts over the test time. As seen in Fig. 12, using the phase and

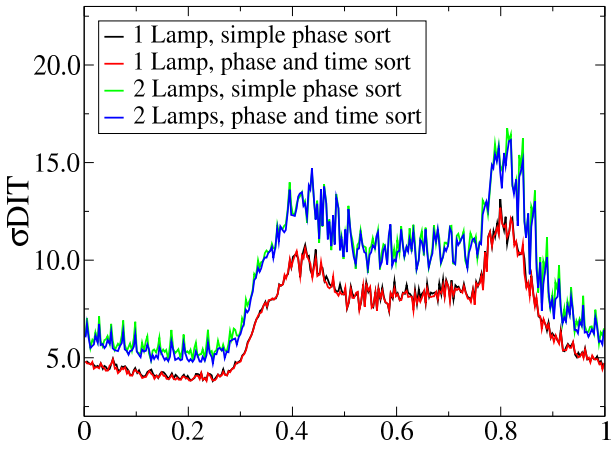

Figure 12: Comparison of a simple phase sort and a phase/time sort. Comparison of different heating schemes, all with 3x3 spatial smoothing using 300 bins over a cycle.

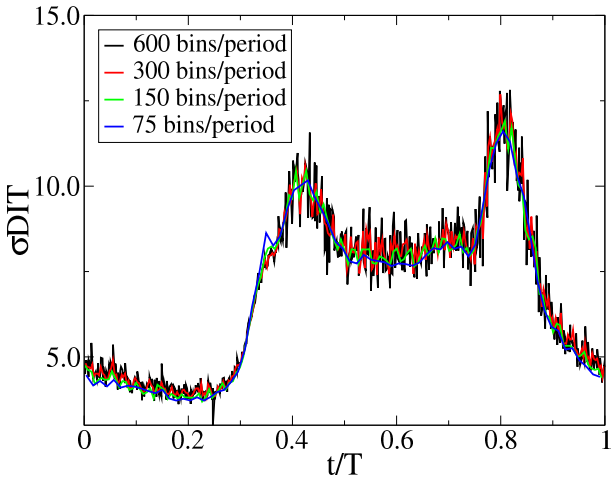

Figure 13: Comparison of the effect of varying the number of bins per cycle with 3x3 spatial smoothing and a phase/time sort.

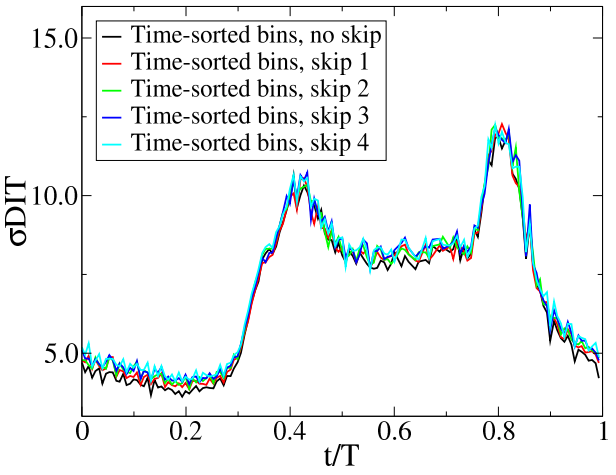

Figure 14: Effect of increasing the time difference between original images used to form DIT images, where the original images are sorted into 150 bins per period.

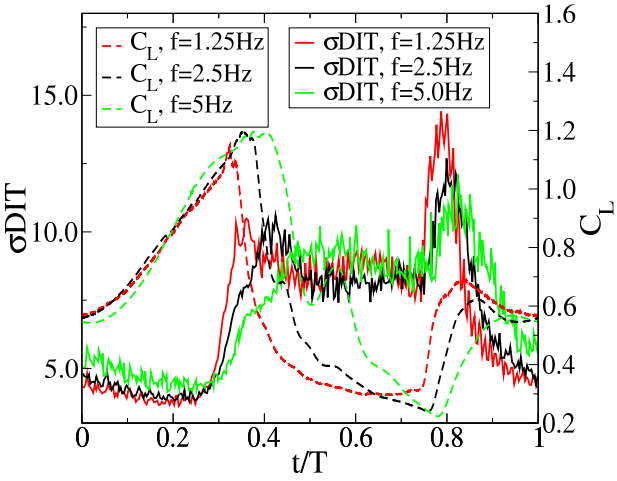

Figure 15: Comparison of the measurement with different pitching frequencies, averaged over the large window with 3x3 spatial smoothing using 300 bins over a cycle.

time sort does result in a slight improvement of the signal to noise ratio over the simple phase sort for the case using two lamps (the signal to noise ratio increases from 3.0 to 3.1), thus for test cases where a significant change in temperature is expected over the test time the phase/time sorting is recommended, and is used for all the reference cases in this paper. The signal to noise ratio is not improved by the additional heating of the second lamp, but the infrared signal increased from 11200 to 11700 counts (+4.5%) and an increase of 5% in the signal to noise ratio is less than could reliably be detected.

Choosing the phase/time sort for further investigations, the effect of varying the number of bins per period is shown in Fig. 13. It can be seen that the main effect is the same as if a running mean or low-pass filter were passed over the data. Since the image movement is not corrected, the maximal pixel movement increases from 0.04 pixels/bin for the case using 600 bins to 0.35 pixels/bin for the case using only 75 bins, which is still around the residual movement remaining after using a derotation algorithm. The effect of alignment errors can be further investigated by sorting the data into 150 bins and changing the time between images used to form the DIT images, thus increasing the movement between DIT images. This method is shown in Fig. 14 for no skipping (reference) and skipping 1,2,3 and 4 intermediate images between the images used to form the DIT image. It can be seen that a small effect is present, reducing the signal to noise ratio from SN=3.0 to SN=2.9 for the worst case, but the total effect is small. In general it can be posited that the alignment does not have a critical effect on the computation of σDIT, but that a gradual reduction in

the signal to noise ratio should be expected with increasing alignment divergence between the two images used for the DIT.

Increasing the airfoil pitching frequency at constant flow speed increases the reduced pitching frequency. As seen in Fig. 15, increasing the pitching frequency delays the dynamic stall to higher angles of attack, and makes the dynamic stall process shorter in absolute time but longer in t/T. The higher pitching frequencies also have higher lift before stall, meaning that more circulation is available to be entrained into the dynamic stall vortex. The flow reattachment is at around the same phase for each of the three pitching frequencies investigated. The σDIT signals show the slowing of the stall process as seen in the lift curves. The σDIT curves are more smoothed at higher frequencies, with the peaks reduced and the base level of σDIT increasing.

When the pitching frequency of the airfoil is changed, this also has an effect on the σDIT. Since the infrared camera frequency and number of images remains constant, the number of infrared images remains constant, and thus there is not a loss in the resolution with which the pitching cycle is resolved. Despite this, the signal-to-noise ratio is worse for higher pitching frequencies (Fig. 15). At the limit of very high pitching frequencies it is clear that the airfoil surface would take on a constant temperature distribution and no signal would result, so increasing the pitching frequency will tend to reduce the signal. A constant trend of reduction in signal to noise ratio is visible from f=1.25 Hz (SN=3.6) through f=2.5 Hz (SN=3.0) to f=5.0 Hz (SN=2.5). Assuming this trend continues, the signal to noise ratio at 20 Hz should be still good at around SN=1.3-1.5, or good measurement values up to a reduced frequency of k=$\pi fc/v_\infty$=0.38 for this carbon fibre surface. The effect of pitching frequency will be dependant on the thermal conductivity and heat capacity of the surface, with more insulating surfaces still being good to higher frequencies.

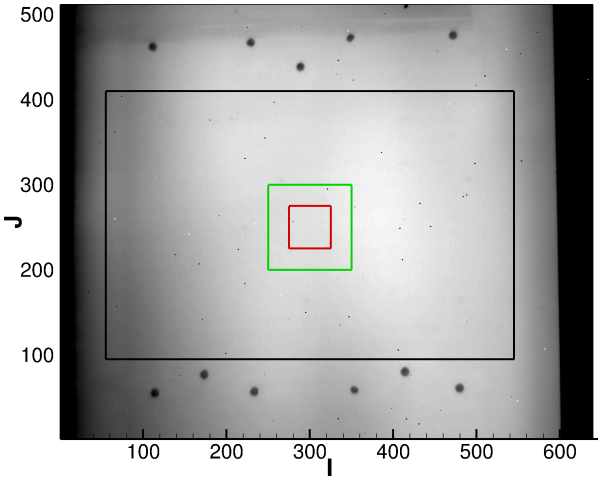

(a)

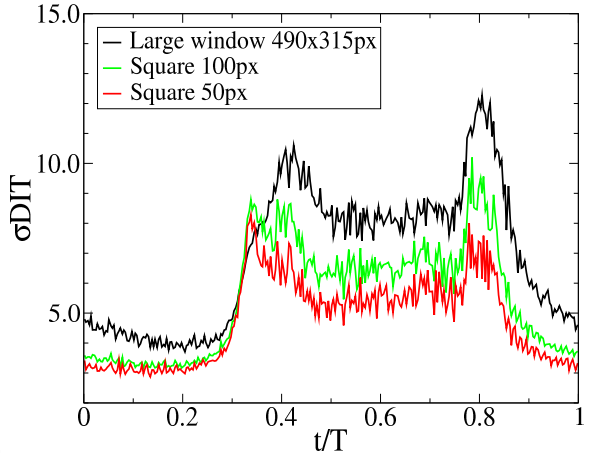

(b)

Figure 16: For the square-shaped windows in (a), in (b) the variation of the σDIT with 3x3 spatial smoothing using 300 bins over a cycle.

6 Effect of interrogation windows

In the classic stall map using tufts, the separation at each tuft can be analysed to give a map of where on the blade at each instant the flow is stalled. Figure 16 shows that for smaller squares it can be seen that the signal to noise ratio is reduced from SN=3.0 to SN=2.8 for the 100x100 px square and to SN=2.3 for the 50x50 px square. Using such squares indicates how the signal to noise ratio becomes worse though insufficient camera resolution, which is always a problem when using infrared cameras on rotors. It can also be seen that the smaller windows deliver more local information, which can be seen in the steeper gradient in σDIT during stall. This opens the possibility of using a moving window technique to analyse the data, so that a surface map of separated/attached flow is generated.

The classical stall map requires knowing whether the rotor blade is stalled or not for each azimuthal angle and radial position. As such it is interesting to know how whether a thin slot-shaped window can be used to evaluate the flow state at different radii. Figure 17 shows the effect of reducing the width of the interrogation window while the length remains the same. Reducing the slot width from 315 pixels to 10 pixels reduces the signal to noise ratio slightly (From SN=3.0 to SN=2.9), but the difference is minimal. A classical stall map should then be no problem. Ordering the windows in slots normal to the flow direction, as in Fig. 18 makes the progression of the stall from trailing edge to leading edge visible. The flow stalls first near the trailing edge in the cyan and blue windows, and last in the black window near the leading edge. A progression in the flow reattachment is also visible, with the black window reattaching first and the reattachment progressing downstream until the cyan window reattaches last. Using this type of slots generates a better signal to noise ratio than for the 50x50 px window (SN=3.1 for the blue window compared to SN=2.3 for the 50x50 px window), probably due to including three times as many pixels in the averaging

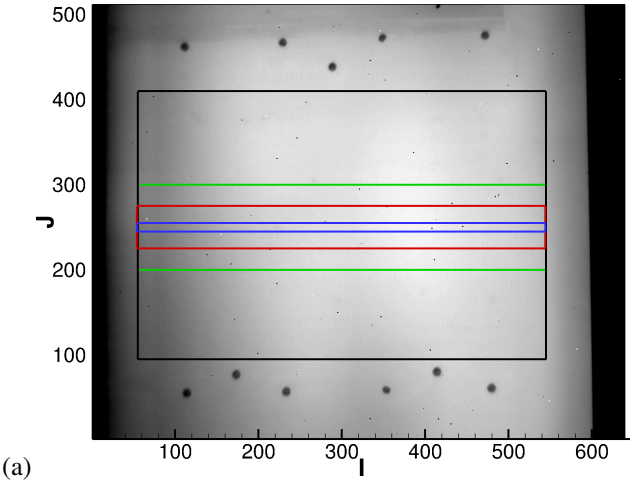

(a)

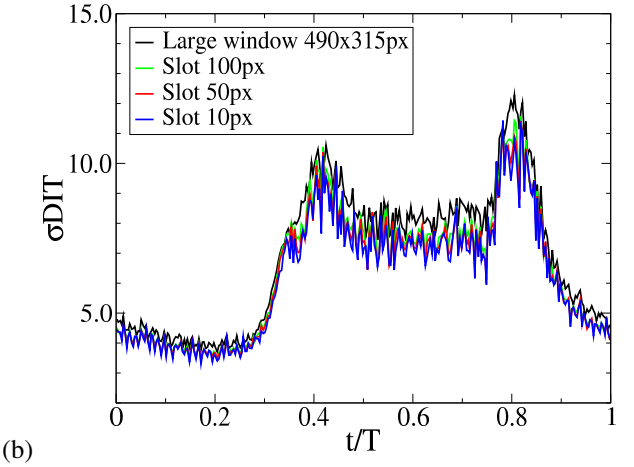

(b)

Figure 17: For the slot-shaped windows in (a), in (b) the variation of the σDIT with 3x3 spatial smoothing using 300 bins over a cycle.

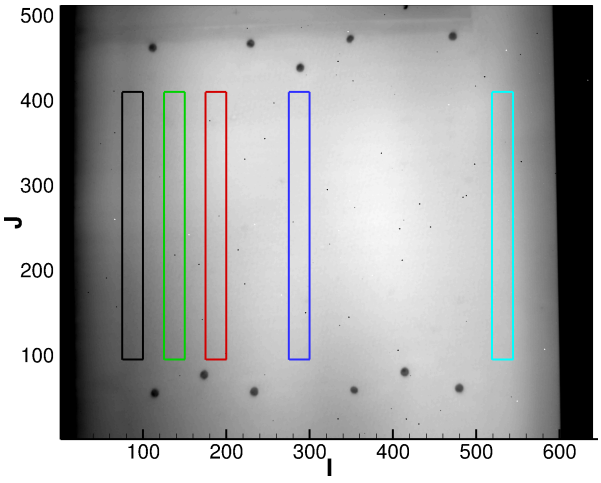

(a)

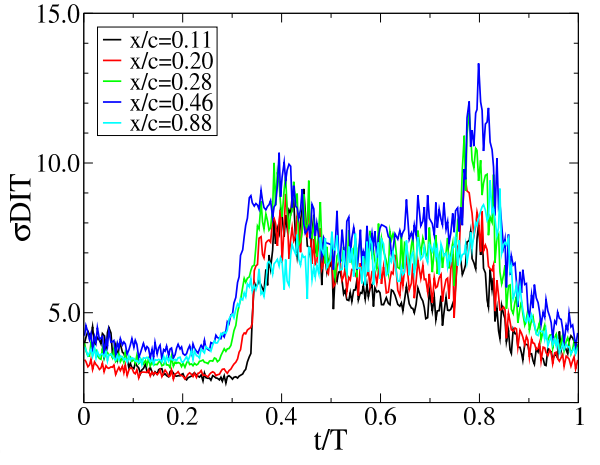

(b)

Figure 18: For the slot-shaped windows of width 25 pixels normal to the flow direction in (a), in (b) the variation of the σDIT with 3x3 spatial smoothing using 300 bins over a cycle.

window.

Using the slot interrogation window allows for a direct comparison between σDIT and σC_P data at the same location, as seen in Fig. 19. It can be seen that, in contrast to the differences in the rise and fall times seen in Fig. 6(a), when the local σDIT is compared that the results are very similar. Both the start and end of dynamic stall is detected at the same point using both techniques, but the plateau during stall is significantly higher for σDIT than for σC_P. Although in this analysis the boundary layer transition was not detected using the IR data, a standard DIT analysis as applied by applied by Raffel et al. [12] will produce the transition positions.

The 50x50 px window can be moved over the image, to provide a spatial evaluation of the DIT images. The windows were moved in steps of 25 px for an overlap in both the x and y directions of 50%. The σDIT images generated in this way can be seen in Fig. 20 to fill a portion of the original image. In Fig. 20, the flow is attached at t/T=0.25, just before the start of flow separation (Compare with Fig. 6). The value of σDIT is not constant over the

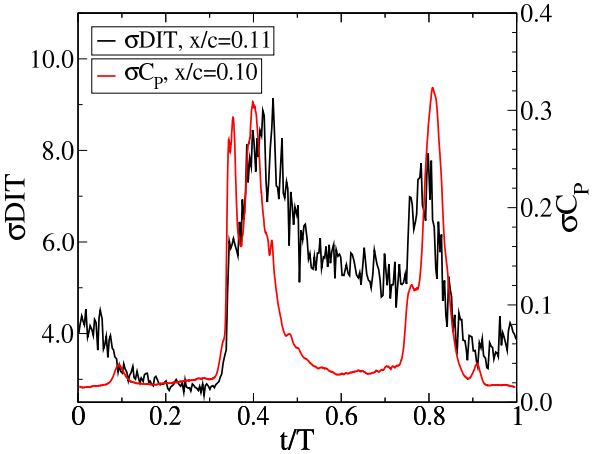

Figure 19: Comparison of σDIT and σC_P at the same location.

image, but at all times σDIT<4. Examining the separation and reattachment processes in Fig. 21, shows that at

t/T=0.30 (Fig. 21a), the separated flow is moving from the top right to the bottom left of the image. The airfoil centerline is at around the top of the raw image, and for an airfoil with free ends the flow will separate first on the airfoil centerline since the effective angle of attack of the airfoil is highest on the centerline and reduces in an elliptical distribution towards the free ends of the airfoil. The movement of the separated flow from trailing edge to leading edge is also noted in the pressure distributions in Fig. 7.

As the trailing edge separation advances toward the leading edge a point is reached where the airfoil is separated, but the suction peak is still preserved. This is seen in pressure distribution (2) in Fig. 7, and in Fig. 21b. The movement of the trailing edge separation pauses from t/T=0.32 to t/T=0.34 before continuing upstream. By t/T=0.35, shown in Fig. 21c, σDIT>5 over the whole airfoil. As seen in Fig. 6 this time is where the slight plateau in σDIT was observed for the whole airfoil. The pressure distributions indicate that this is when the leading edge dynamic stall vortex is formed and starts to propagate downstream. The images with the moving window after t/T=0.35 do not show the motion of the dynamic stall vortex, but remain at a high level of σDIT. After the dynamic stall process the airfoil presents fully stalled flow which is similar to that seen for the static stall case, and Fig. 21d shows a similar non-uniform σDIT distribution to that seen for the attached flow, but with a mean level of around σDIT=4.5. This situation remains until the start of the reattachment process.

Figure 21e shows the early phase of the reattachment process at t/T=0.83, with reattaching flow moving from the leading edge to the trailing edge. This process is also visible in an analysis of the pressure sensor data (not shown), as the suction peak reestablishes before the flow at the trailing edge is reattached. The final snapshot in Fig. 21f shows the progress of the flow reattachment at t/T=0.856, and by t/T=0.88 the flow is reattached and the σDIT image is again similar to that for the attached flow in Fig. 20. The method of using a moving evaluation window is a powerful analysis technique showing the spatial separation and reattachment processes on the airfoil. The technique depends on having sufficient pixels in the evaluation window to increase the signal to noise ratio to an acceptable level. It can be envisaged that in the future with high-resolution IR cameras that the moving window method will be a practical technique for wind tunnel analysis. Where lower numbers of pixels are available, the single window evaluation method will probably be preferable.

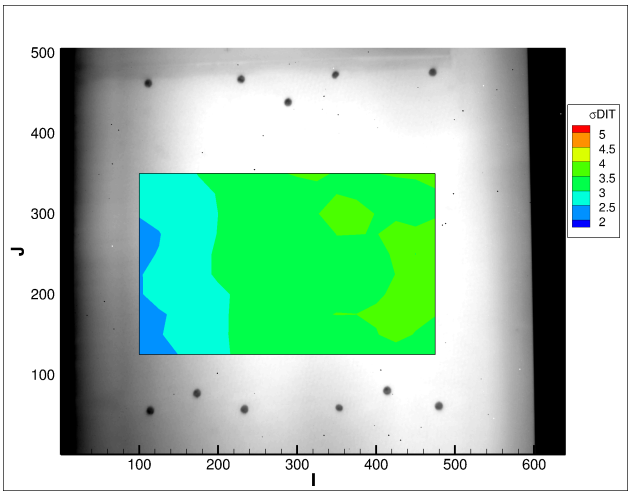

Figure 20: Data from the moving 50x50 px window with 25 px overlap at t/T=0.25 showing the position of the data window

7 Conclusion

A new method of detecting flow separation for static and pitching airfoils is described. The method is robust and does not require contact with the surface, any kind of surface treatment or instrumentation and can produce maps of the surface on which stalled and unstalled areas are detailed. The important results are:

- A high-speed infrared camera is used and then difference images (DIT) between consecutive images are formed. A cut-out window is defined, and in that window the standard deviation is computed to form a single value, σDIT.
- σDIT is high for separated flow and low for attached flow and this could be verified by comparison to unsteady pressure distributions.
- The paper describes methods of enhancing the signal to noise ratio of the images using filtering, sorting and window selection methods, and the signal-to-noise ratio could be improved to SN=3.6, however even the unfiltered data had a signal to noise ratio of 1.8, which is usable.
- The method works both for a statically inclined airfoil and a pitching airfoil which was tested up to a pitching frequency of 5 Hz. Extrapolations suggest that data could be extracted from the airfoil tested at leat up to 20 Hz, but this value will be dependant on the thermal properties of the airfoil surface.
- Using a moving window produced spatially resolved stall maps of the surface which could be verified by comparison to pressure distributions.

This new use for highly resolving and fast IR cameras in aerodynamic research has also been tested for a rotating dynamically pitching airfoil in the rotor test stand (RTG) of the DLR in Göttingen [18], with encouraging initial results.

8 Acknowledgments

The authors are grateful for the assistance of Markus Krebs and Christoph Merz during the experiments.

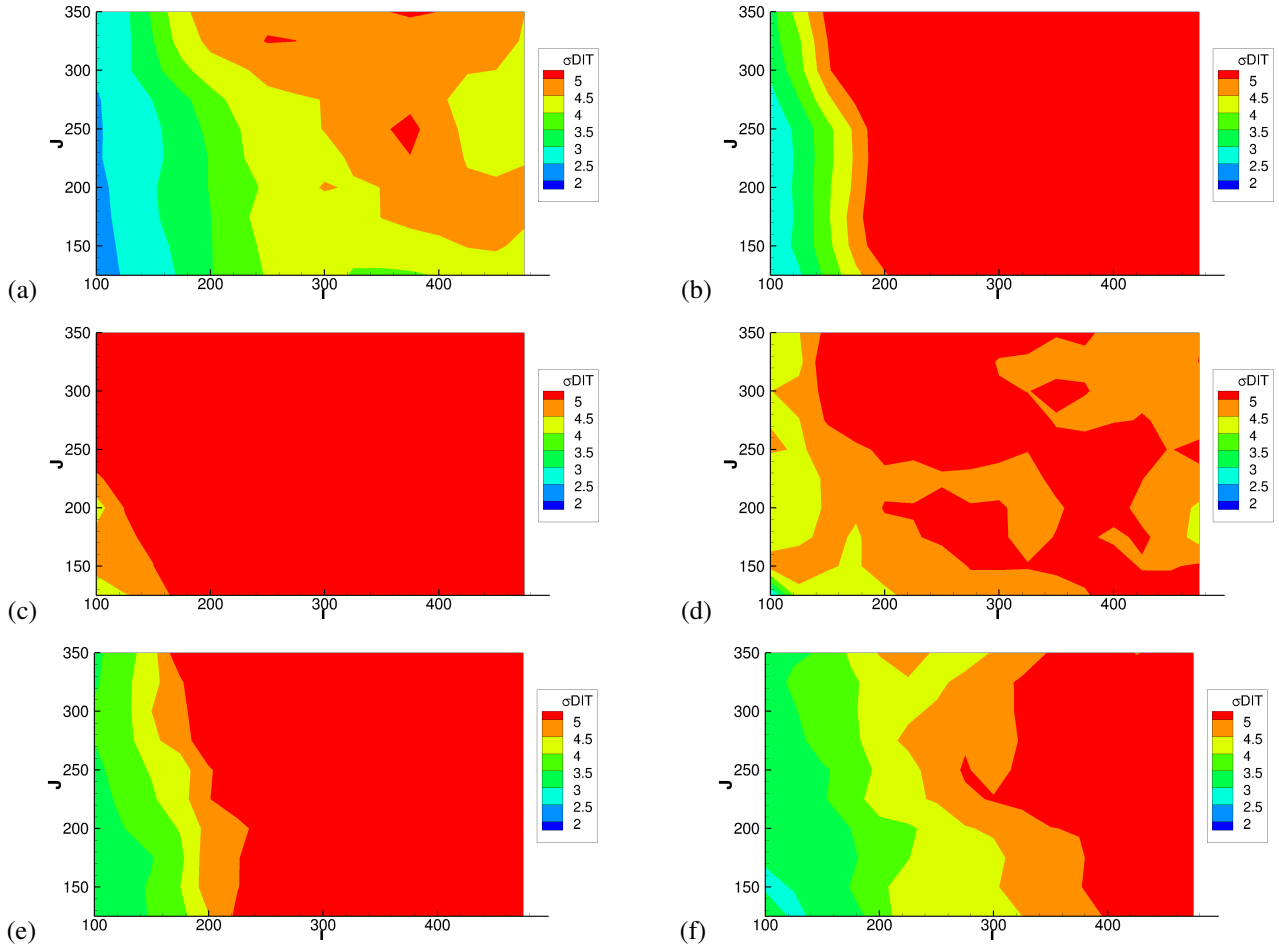

Figure 21: Data from the moving 50x50 px window: (a) t/T=0.30, (b) t/T=0.32, (c) t/T=0.35, (d) t/T=0.50, (e) t/T=0.83, (f) t/T=0.856.

References

[1] Astarita, T., Cardone, G., "Thermofluidynamic analysis of the flow in a sharp 180 degrees turn channel", *Experimental Thermal and Fluid Science*, Vol. 20, No. 3-4, 2000, pp188-200

[2] Bouchardy, A.-M., Durand, G., Gauffre, G., "Processing of Infrared Thermal Images for Aerodynamic Research", *Applications of Digital Image Processing*, Vol. 397, April 1983, pp. 304-309.

[3] Bousman, W. G., "A Qualitative Examination of Dynamic Stall from Flight Test Data", *Journal of the American Helicopter Society*, Vol. 43, No. 4, 1998, pp. 279-295

[4] Carlomagno, G. M., Cardone, G., "Infrared thermography for convective heat transfer measurements", *Experiments in Fluids*, Vol. 49, No. 6, 2010, pp. 1187-1218

[5] de Luca, L., Carlomagno, G.M., Buresti, G. "Boundary-layer diagnostics by means of an infrared scanning radiometer", *Experiments in Fluids*, Vol. 9, No. 3, 1990, pp. 121-128

[6] Disotell, K.J., Peng, D., Juliano, T.J., Gregory, J.W., Crafton, J.W., Komerath, N.M., "Single-shot temperature- and pressure-sensitive paint measurements on an unsteady helicopter blade", *Experiments in Fluids*, Vol. 55, No. 2, 2014. DOI:10.1007/s00348-014-1671-2

[7] Gardner, A.D., Richter, K., "Boundary layer transition determination for periodic and static flows using phase-averaged pressure data", *Experiments in Fluids*, Vol. 56, No. 6, 2015. DOI: 10.1007/s00348-015-1992-9

[8] Gartenberg, E., Roberts, A.S. Jr. "Twenty-Five Years of Aerodynamic Research with Infrared Imaging", *Journal of Aircraft*, Vol. 29, No. 2, 1992, pp161-171.

[9] Gustafson, F. B., Myers, G. C., Jr., "Stalling of Helicopter Blades", NACA Report No. 840, April 1946.

[10] Mulleners, K., Kindler, K., Raffel, M., "Dynamic stall on a fully equipped helicopter model", Aerospace Science and Technology 19, S. 72-76, 2012. DOI:10.1016/j.ast.2011.03.013

[11] Quast, A., "Detection of Transition by Infrared Image Technique" In: 12th international congress on instrumentation in aerospace simulation facilities (ICIASF 87), Williamsburg, VA, 22-25 June 1987, pp. 125-134

[12] Raffel, M., Merz, C.B, Schwermer, T., Richter, K., “Differential infrared thermography for boundary layer transition detection on pitching rotor blade models”, *Experiments in Fluids*, Vol. 56, No., 2, 2015, DOI 10.1007/s00348-015-1905-y

[13] Raffel, M., Gardner, A.D., Schwermer, T., Merz, C.B., Weiss, A., Braukmann, J, Wolf, C.C., Ewers, B., “Differential Infrared Thermography (DIT) for Dynamic Stall Detection”, 18th International Symposium on Applications of Laser Techniques to Fluid Mechanics Lisbon, Portugal, 04-07 July, 2016, submitted to *Experiments in Fluids*

[14] Ricci, R., Montelpare, S., “A quantitative IR thermographic method to study the laminar separation bubble phenomenon”, *International Journal of Thermal Sciences*, Vol. 44, No. 8, 2005, pp709-719

[15] Richter, K., Wolf, C.C., Gardner, A.D., Merz, C.B, “Detection of Unsteady Boundary Layer Transition Using Three Experimental Methods”, AIAA-2016-1072, AIAA SciTech 2016, 54th AIAA Aerospace Sciences Meeting, San Diego (CA), USA, 4-8 January 2016

[16] Richter, K., Koch, S., Goerttler, A., Lütke, B., Wolf, C.C., Benkel, A., “Unsteady Boundary Layer Transition on the DSA-9A Rotor Blade Airfoil”, 41st European Rotorcraft Forum, Munich, Germany, 1-4 Sept. 2015.

[17] Richter, K., Schülein, S., “Boundary-layer transition measurements on hovering helicopter rotors by infrared thermography”, *Experiments in Fluids*, Volume 55, Issue 7, July 2014. DOI: 10.1007/s00348-014-1755-z

[18] Schwermer, T., Richter, K., Raffel, M., “Development of a Rotor Test Facility for the Investigation of Dynamic Stall”, In: New Results in Numerical and Experimental Fluid Mechanics X, Notes on Numerical Fluid Mechanics and Multidisciplinary Design Volume 132, 2016, pp 663-673. DOI: 10.1007/978-3-319-27279-5_58

[19] Simon, B., Filius, A., Tropea, C., Grundmann, S., “IR thermography for dynamic detection of laminar-turbulent transition”, *Experiments in Fluids*, Volume 57, Issue 5, May 2016. DOI: 10.1007/s00348-016-2178-9

[20] Thomann, H., and Frisk, B., “Measurement of Heat Transfer with an Infrared Camera”, *International Journal of Heat and Mass Transfer*, Vol. 11, 1968, pp. 819-826.